MSEC2019-2983

BINDER JETTING ADDITIVE MANUFACTURING OF CERAMICS: COMPARISON OF FLOWABILITY AND SINTERABILITY BETWEEN RAW AND GRANULATED POWDERS

Wenchao Du
Department of Industrial & Systems Engineering
Texas A&M University
College Station, TX 77843

Guanxiong Miao
Department of Mechanical Engineering
Texas A&M University
College Station, TX 77843

Lianlian Liu
Department of Materials Science & Engineering
Texas A&M University
College Station, TX 77843

Zhijian Pei
Department of Industrial & Systems Engineering
Texas A&M University
College Station, TX 77843

Chao Ma
Department of Engineering Technology & Industrial Distribution
Department of Industrial & Systems Engineering
Department of Mechanical Engineering
Department of Materials Science & Engineering
Texas A&M University
College Station, TX 77843

ABSTRACT

The objective of this study is to compare three different feedstock powders for the binder jetting process by characterizing their flowability and sinterability. Binder jetting additive manufacturing is a promising technology for fabricating ceramic parts with complex or customized geometries. Granulation is a promising material preparation method due to the potential high sinterability and flowability of the produced powder. However, no study has been made to systematically compare raw and granulated powders in terms of their flowing and sintering behaviors. This paper aims at filling this knowledge gap. Two raw powders (i.e., fine raw powder of 300 nm and coarse raw powder of 70 μm) and one granulated powder from spray freeze drying were compared. Different flowability metrics, including volumetric flow rate, mass flow rate, Hausner ratio, Carr index, and repose angle were measured. Different sinterability metrics, including sintered bulk density, volume shrinkage, and densification ratio were compared for all three powders. Results show that granulated powder achieved comparably high flowability to that of the coarse raw powder and also comparably high sinterability to that of the fine raw powder. Moreover, suitable metrics for the characterization of the sinterability and flowability for these three powders are recommended. This study suggests spray freeze drying produces high-quality feedstock powder for binder jetting process.

1. INTRODUCTION

Ceramic materials have outstanding properties, such as extraordinary hardness, excellent resistance to wear, heat, and corrosion, and exceptional biocompatibility [1]. However, it is very costly to fabricate ceramic parts of complex shapes using conventional manufacturing techniques. For complex ceramic parts, tooling can contribute to up to 80 % of the overall cost if traditional processing routes are taken [2]. Compared with that, additive manufacturing (AM), also known as 3D printing, has many advantages, including elimination of special fabrication tooling, flexible and customized design, and efficient usage of raw materials. Therefore, AM of ceramic materials have attracted a lot of research interest [3]. Among all AM technologies, binder jetting is considered the most promising for printing ceramic materials because it is easy to scale up and it does not require support [4], which has been extensively investigated in the field of ceramics to fabricate structural, functional, and biomedical parts [4–13]. Currently, the bulk density [14] of sintered ceramic parts by this process ranges from 40% to 68% [15–20], far below the requirement for load-bearing applications. The main cause comes from the contradicting requirements for the particle size of the feedstock powder: a large

particle size (>5 μm) is required for a high flowability while a small particle size (<1 μm) for a high sinterability.

Powder granulation is a suitable method when feedstock powder with high flowability and high sinterability is required [1]. Popular granulation technologies include manual mixing and grinding [21], spraying drying (SD) [22–24], and spray freeze drying (SFD) [25–27]. Manual mixing and grinding can prepare irregular granules; on the contrary, SD and SFD usually produce spherical granules. Moreover, SD possesses unique characteristics such as rapid water evaporation, continuous operation, and high production rate [28], and SFD can produce structurally homogeneous granules [25].

Suwanprateeb et al. [21] studied two granulated hydroxyapatite powders for binder jetting, i.e., manually granulated powder and SD powder. Mass flow rates of these two powders were measured and compared. It was shown that SD powder achieved higher flow rate because of its spherical shape. Green bulk density and sintered bulk density were also characterized for the pressed disk samples from these two powders. It was found that manually granulated powder achieved much higher green and sintered bulk densities than the SD powder. Irsen et al. compared two granulated hydroxyapatite powders from SD and fluidized bed granulation with the raw powder [29]. By characterizing the apparent density, tap density, and mass flow rate, SD granulated powder was chosen to perform the binder jetting printing due to its spherical shape and good flowability.

Despite some existing studies on the feedstock powder comparison for the binder jetting process, no research has been done to compare the granulated powder with raw solid powders regarding their flowability and sinterability using various metrics. In this study, a granulated powder made from SFD was prepared from fine raw powder. Three different powders, including the fine raw powder, coarse raw powder, and granulated powder, were characterized with scanning electron microscope, and their flowability and sinterability were measured and compared by various metrics. Suitable metrics for the flowability and sinterability of the feedstock powder for binder jetting are recommended.

2. EXPERIMENTAL METHODS

2.1 Materials

Fine alumina powder (300 nm, Allied High Tech, CA, USA) was used as the fine raw powder, and coarse spherical alumina powder (70 μm, Inframat, CT, USA) were used to be the coarse raw powder.

2.2 Spray freeze drying

The fine alumina powder was used for the slurry preparation, whose parameters are shown in Table 1. The preparation started with adding water and alumina balls into a high-density polyethylene bottle. To decrease the slurry viscosity, an ammonium salt of an acrylic polymer (Dispex AA 4040 NS, BASF, Germany) was added as dispersant, followed by a manual shaking to evenly mix the dispersant with the water. Half the amount of the powder was then added, and the mixture was ball-milled (Laboratory Jar Rolling Mill, Paul O. Abbe, IL,

USA). The remaining powder was evenly separated into five portions, and each portion was added into the bottle once every hour. After all powder was added, the ball milling continued for 12 h. Then a sieve with an opening size of 250 μm was used to filter the slurry into a beaker to be ready to spray.

Table 1. The parameters for the slurry preparation

Parameter	Value
Alumina solid loading (vol. %)	20
Dispersant-to-powder weight ratio	0.015:1
Ball diameter (mm)	6.35
Ball-to-slurry weight ratio	1:1

The spray freeze drying includes spray freezing and freeze drying. Figure 1 shows the machine (LS-2, PowderPro AB, Sweden) for the spray freezing. A peristaltic pump feeds the slurry into an atomizing nozzle, which is connected with compressed air. The slurry is atomized into droplets, which are sprayed into liquid nitrogen in the spraying container and frozen. The frozen granules are then lyophilized on a tray in the drying chamber of the freeze drier (FreeZone 2.5 L, Labconco, MO, USA). The tray can be heated to speed the lyophilization. The parameters for spraying freezing and freeze drying are shown in Table 2. Obtained granulated powder was sieved to 53–90 μm by a digital sieve shaker (AS 200, Retsch GmbH, Germany).
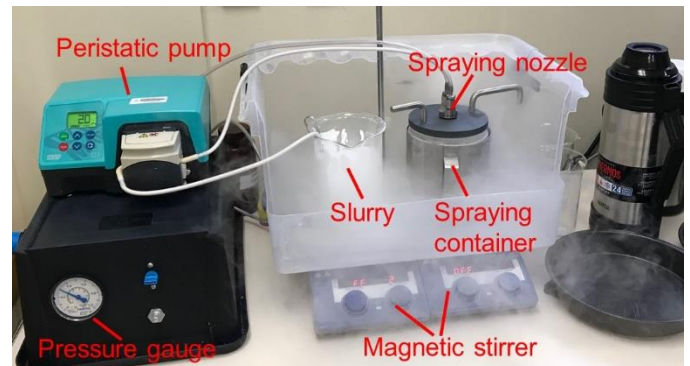

Figure 1. PowderPro LS-2 freeze granulator

Table 2. The parameters for spray freezing and freeze drying

Process	Parameter	Value
Spray freezing	Spraying pressure (bar)	0.3
	Feed rate (L/h)	0.5
Freeze drying	Vacuum (mbar)	1.5
	Tray temperature (°C)	20
	Collector temperature (°C)	-50
	Drying time (h)	12

2.3 Material characterization

Scanning electron microscopy (SEM, TESCAN VEGA II LSU, Brno-Kohoutovice, Czech Republic) was used to characterize the morphologies of the fine raw powder, coarse raw powder, and granulated powder. To prepare the sample for the morphology of the fine raw powder after milling, the slurry was

diluted and dripped onto the surface of a silicon wafer, which was left at room temperature to be slowly dried.

Particle sizes of the coarse raw powder and the granulated powder were analyzed based on the SEM images by ImageJ, which is an open-source software for image analysis. Its volume-weighted mean size D was obtained based on the following equation [30]:

$$D = \frac{\sum_n^{i=1} D_i \cdot V_i}{\sum_n^{i=1} V_i} \tag{1}$$

where n is the number of the particles in the SEM image, D_i and V_i are the diameter and volume of Particle i, respectively.

2.4 Flowability measurement

Five different flowability metrics, i.e., volumetric flow rate (FR_v), mass flow rate (FR_m), Huasner ratio (HR), Carr index (CI), and repose angle (RA) were tested for all three powders. All measurements were carried out based on three test portions. The volumetric (mass) flow rate, i.e., the volume (mass) of falling granules through a funnel with an opening of $\Phi2.54$ mm in one second, was tested by a Hall flowmeter (DF-1-02, Hongtuo, China). The measurement started with filling the funnel with the powder until it overflowed from the periphery of the funnel. Then the powder above the top surface was wiped off by a spatula, followed by weighting the powder and the funnel. The time that the powder completely passed through the funnel and the weight of the empty funnel were recorded.

The Hausner ratio (HR) [1] and Carr index (CI) [31] are defined by the following equations

$$HR = \frac{\rho_t}{\rho_a} \tag{2}$$

$$CI = 100\left(1 - \frac{\rho_a}{\rho_t}\right) \tag{3}$$

where ρ_t and ρ_a are the tap density (the density of powder after a certain number of tapping cycles) and the apparent density (the density of freely settled powder). The tapped density of each powder was measured by putting 50 mL powder into a glass cylinder with a 100 mL capacity. 3000 taps were applied for each measurement with a tap stroke of 3 mm. The apparent densities of the coarse raw powder and granulated powder were obtained by a Hall flowmeter funnel [32]. As fine raw powder has a low flowability and cannot freely flow through the Hall flowmeter funnel, the Carney funnel, which has a larger opening, was chosen to test its apparent density [33].

As the coarse raw powder showed the best flowability in this study, its value is set as the baseline to obtain the normalized value of the each flowability metric. For example, the normalized volumetric flow rate of granulated powder (FR'_{vg}) was obtained by the following equation:

$$FR'_{vg} = \frac{FR_{vg}}{FR_{vc}} \times 100\%$$

where FR_{vg} is the volumetric flow rate of the granulated powder and FR_{vc} is the baseline value (i.e., the volumetric flow rate of the coarse raw powder).

2.5 Sinterability measurement

The sinterability of all three powders was characterized by three different metrics, including sintered bulk density, volumetric shrinkage, and densification ratio [1]. Three samples were prepared for each powder. For each sample, 1 g powder was dry-pressed at 100 MPa into a cylindrical disk of $\Phi12.7$ mm by a hydraulic cold press (Carver Laboratory Press, Model C, Fred S. Carver Inc., IN, USA). The pressed sample from the coarse raw powder collapsed after pressing. Therefore, an aqueous solution containing 3 wt. % polyvinyl alcohol (PVA, 363138, Sigma-Aldrich, MO, USA) was added as a binder. Since the PVA percentage is low, its effect on the sintering could be neglected. The coarse raw powder and the binder solution were mixed to achieve a desired alumina-to-PVA weight ratio of 99.5:0.5. Then the mixed coarse powder was put in an oven with a temperature of 60 °C for 0.5 h to evaporate the water, followed by the die pressing. The green disk samples from all three powders were sintered at 1600 °C for 2 h and cooled to the room temperature in a bench-top muffle furnace (KSL-1700X-A1-UL, MTI Corp., CA, USA).

Table 3. Equations for sinterability metrics

Variable	Symbol	Equation
Bulk volume of green sample (cm³)	V_g	$\dfrac{\pi d_g^2 t_g}{4}$
Bulk volume of sintered sample (cm³)	V_s	$\dfrac{m_{s3} - m_{s2}}{\rho_{wt}}$
Relative bulk density of the green sample (%)	ρ_g	$\dfrac{4m_g}{\pi d_g^2 t_g} \times 100$
Volumetric shrinkage (%)	S_v	$\left(1 - \dfrac{V_s}{V_g}\right) \times 100$
Relative bulk density of the sintered sample (%)	ρ_s	$\dfrac{\rho_{wt}}{\rho_{th}} \cdot \dfrac{m_{s1}}{m_{s3} - m_{s2}} \times 100$
Densification ratio (%)	R_d	$\dfrac{\rho_s - \rho_g}{1 - \rho_g} \times 100$

The weight (m_g) of the green disk sample was measured by a balance and the diameter (d_g) and thickness (t_g) were measured by calipers. The relative bulk density of the green samples was calculated based on the dimension and the weight of the green disk samples. As geometry-based calculation of the sintered volume of the disk samples is not accurate due to the nonhomogeneous shrinkage during sintering, the sintered volume and relative sintered bulk density of the disk samples were measured by a density kit (Torbal AGCN200, Scientific Industries Inc., NJ, USA) based on an ISO standard [14]. Specifically, dry sintered weight (m_{s1}) was measured after sintering and cooling. Then the sample was boiled in deionized water for 2 h and then cooled to the room temperature. The sintered weight in water (m_{s2}) was measured and the sample was wiped by a wet cloth. The weight of the wiped sample (m_{s3}) was measured. The volumetric shrinkage, relative sintered bulk density, and densification ratio of the sample were calculated

based on the equations in Table 3, where ρ_{wt} is the water density at the temperature when taking the measurement.

3. RESULTS AND DISCUSSION

3.1 Material morphology and size

The top row of Figure 2 shows SEM images of the fine raw powder before ball milling, which consists of irregular agglomerates with a wide size range. After ball milling, some small agglomerates still exist, but most of the large agglomerates were crushed into nanoparticles, as shown in the bottom row of Figure 2.
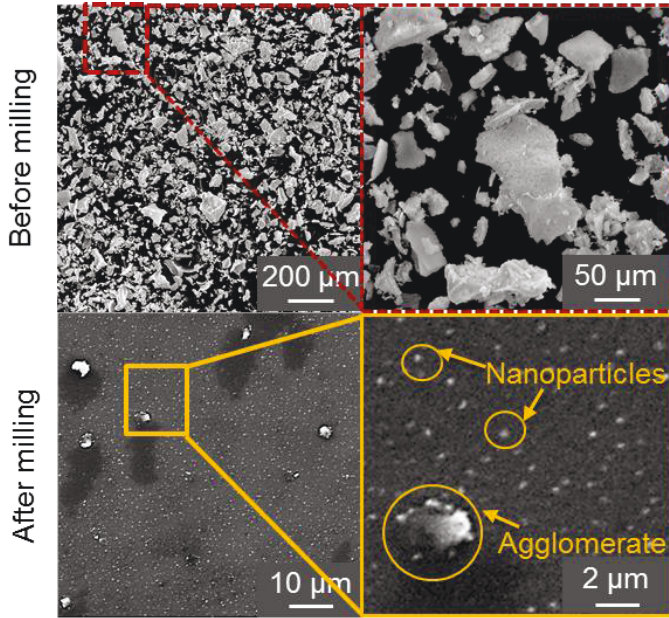

Figure 2. SEM of fine raw powder before and after ball milling

The morphology of the coarse raw powder and the granulated powder is shown in Figure 3. Both are almost perfectly spherical. The particle size distributions are shown in Figure 4. As the granulated powder is sieved to conform its size to that of the coarse raw powder, its size distribution is narrower than that of the coarse raw powder. The calculated mean particle sizes from Eq. 1 for the coarse raw and granulated powder are 77.4 µm and 69.2 µm, respectively.

3.2 Flowability

The measured apparent densities and tap densities of the three powders are shown in Table 4. The standard deviation of each result was based on three measurements. The granulated powder possesses higher apparent density than the fine raw powder. Examination of the forces applied on the particles is needed to explain this result. As the inter-particle force, such as van de Waals and electricstatic force, is dominant for fine particles [34], it has a greater extent of agglomeration than that of the coarse particles. For the fine raw powder (300 nm), the agglomeration is severe (as shown in Figure 2), resulting in a much loose packing. Moreover, significant inter-agglomerate friction due to the irregular shape also restricts the powder packing and therefore led to the low apparent density of the fine

raw powder. Even after tapping, the severe agglomeration still led to a lower tapped density than the granulated powder.
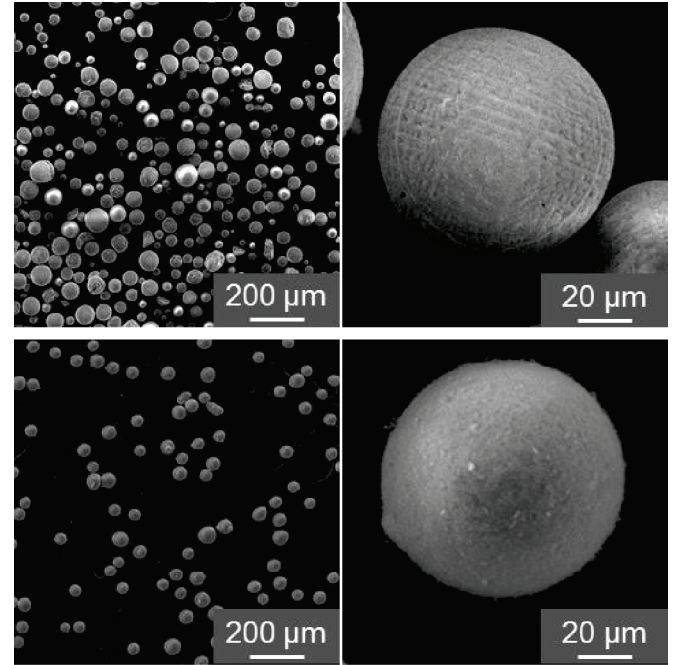

Figure 3. SEM of the coarse raw powder (top row) and the granulated powder (bottom row)
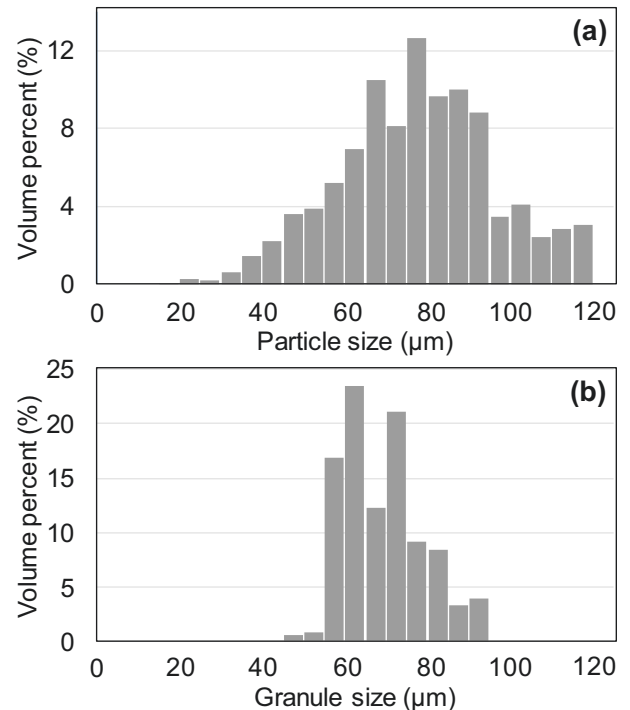

Figure 4. Particle size distribution of the coarse raw powder (a) and the granulated powder (b)

The granulated powder possesses lower apparent density and tap density than the coarse raw powder. This results from the internal structure of the granulated powder. As the solid loading

of the slurry for the spray freezing is 20 vol. %, a large number of ice dendrites nucleated in the frozen granules. After lyophilization, pores were left in the internal structure of the granules. Therefore, the density of each granule is much lower than that of a solid particle. It can be assumed the density of each granule is around 20% because the ceramic concentration of the slurry is 20 vol.% and there is no significant volume change during the freezing and drying. This is why the apparent and tap densities of the granulated powder is about 20% of those of the course raw powder, respectively.

Table 4. The apparent density and tap density for the three powders

Powder	Apparent density (%)	Tap density (%)
Raw fine	7.2±0.1	13.8±0.3
Raw coarse	52.6±0.4	59.8±0.5
Granulated	11.6±0.6	14.2±0.2

The volumetric and mass flow rates, Hausner ratio, Carr index, and the repose angle of the three powders are shown in Table 5 as with the standard deviation based on three measurements. As they both used the same volume of powder, volumetric flow rate of the coarse raw powder is about twice as large as that of the granulated powder. The mass of a full funnel of the coarse raw powder (117.78±0.01 g) is much larger than that of the granulated powder (25.96±0.01 g), resulting in a mass flow rate of ten times as large as that of the granulated powder. Compared with the lag of the volumetric flow rates, the larger lag of the mass flow rate of the granulated powder attributes to its low inner-granule density and low granule packing density. Due to the dominant inter-particle forces and large inter-agglomerate/particle friction, the fine raw powder cannot fall through the funnel opening and its flow rate values could not be measured. Therefore, flow rate is not a suitable metric to characterize the flowability of the fine raw powder.

As shown in Table 5, the flowabilities of all three powders were successfully quantified by the Hausner ratio, Carr index, and repose angle. The smaller the Hausner ratio (closer to one), the better the flowability. Both the coarse raw and granulated powders achieved relative small Hausner ratio values, while the fine raw powder obtained a relatively large Hausner ratio. For the Carr index, the same rule applies: the smaller the Carr index, the better the flowability. Similar trends were observed on Carr index. The value for the coarse raw powder is the smallest, followed by that of the granulated powder. The fine raw powder achieved the largest Carr index.

The smaller the repose angle, the better the flowability of the tested powder. Figure 5 shows the repose angles of the three powders. As the fine raw powder has significnat inter-particle forces and thus a great extent of agglomeration, it possesses higher inter-agglomerate friction due to the irregular shape of the agglomerates. As shown in Figure 5, the repose angle of fine raw powder is larger than that of the other two powders. Granulated powder achieved a close repose angle to the coarse raw powder, indicating similar flowabilities between each other.

Table 5. Flowability metric values for three powders

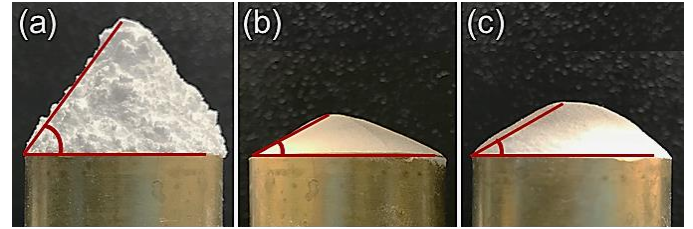| Metric	Fine raw powder	Coarse raw powder	Granulated powder
Volumetric flow rate (cm^3/s)	/	0.70±0.01	0.30±0.01
Mass flow rate (g/s)	/	1.54±0.01	0.15±0.01
Hausner ratio	1.8±0.1	1.1±0.0	1.2±0.1
Carr index	48.2±1.2	12.3±0.1	18.7±1.1
Repose angle (º)	51.7±3.9	25.3±1.6	29.5±1.1

Figure 5. Measurements of repose angle for fine raw powder (a), coarse raw powder (b), and granulated powder (c)
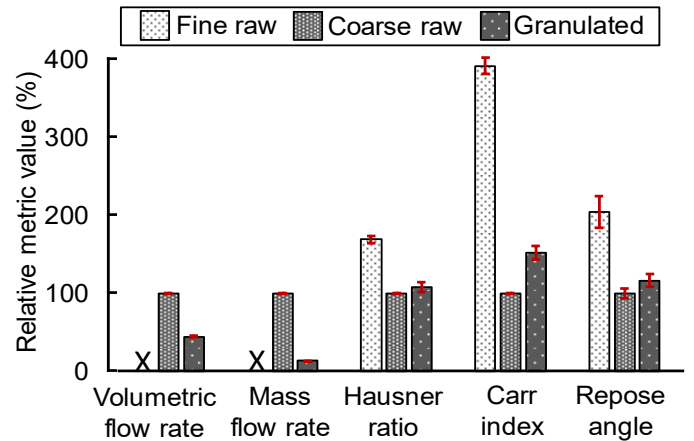

Figure 6. Normalized values for different flowability metrics (Cross sign means there is no available value)

The normalized values for the five flowability metrics are shown in Figure 6. For volumetric and mass flow rates, large value means good flowability, while low values indicate good flowability for the Hausner ratio, Carr index, and repose angle. All normalized metric values for coarse raw powder are 100 % as they are the baseline values.

In summary, the granulated powder achieved comparable flowability metric values of Hauser ratio, Carr index, and repose angles to the coarse raw powder, indicating its good flowability. The flowability of the fine raw powder is much lower than those of other two powders. Volumetric and mass flow rates are not suitable metrics to characterize the flowability of fine raw powder as it could not flow through the funnel.

3.3 Sinterability

The green bulk density, sintered bulk density, volumetric shrinkage, and the densification ratio for all three powders are shown in Table 6 and Figure 7, in which the standard deviation

was based on three measurements. The pressed disk samples from the coarse raw powder achieved the highest green bulk density of 59.7±1.9%, resulting from the dominance of the gravity among the forces applied on the coarse raw particles and consequently a dense packing. Moreover, its spherical shape promoted the compacting movement of the particles. On the contrary, disk pressing of the fine raw powder was hindered by the significant inter-particle forces and the samples achieved the lowest green bulk density. Although the granulated powder was made from the fine raw powder, the spherical shape and the larger size helped improve the flowability and thus green density.

The particle size of the ceramic material is an important variable affecting sinterability [35]. Under the same conditions, a powder with a smaller particle size has a higher sintering driving force. Therefore, more significant densification occurred during sintering [35,36] of the fine raw and the granulated powder than the coarse raw powder, leading to higher sintered densities.

Volumetric shrinkage and the densification ratio were determined from the green density and the sintered density. The samples from the fine raw powder and the granulated powder achieved large volumetric shrinkage, indicating the high sinterability of these two powders. Only limited volumetric shrinkage occurred for the coarse raw powder, suggesting the low sinterability of the coarse raw powder. Similarly, the fine raw powder and granulated powder achieved much higher densification ratios than the coarse raw powder.

In summary, the granulated powder achieved a sintered bulk density, volumetric shrinkage, and densification ratio close to those of the fine raw powder, indicating that the good sinterability of the fine powder was maintained after the granulation. All sinterability metrics of the coarse raw powder are lower than those of the fine raw powder and the granulated powder, especially for the volumetric shrinkage and densification ratio. Therefore, it is concluded that the sinterability of the coarse raw powder is much lower than those of the other two powders. Moreover, sintered bulk density is not suitable to characterize the sinterability of coarse raw powder as it strongly depends on the green bulk density.

Table 6. Sinterability metric values for three powders

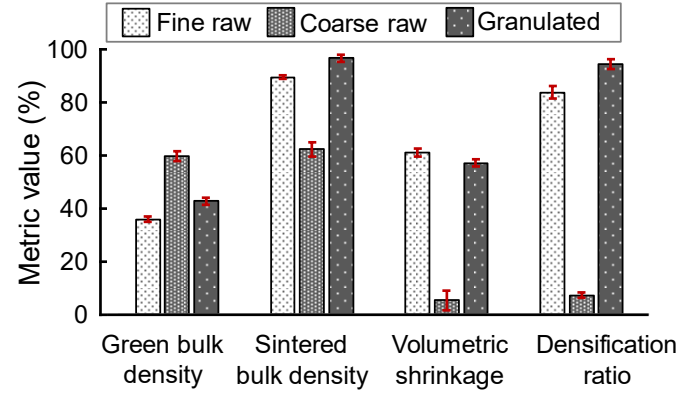| Metric	Fine raw powder	Coarse raw powder	Granulated powder
Green bulk density (%)	35.9±1.0	59.7±1.9	42.8±1.3
Sintered bulk density (%)	89.7±0.8	62.4±2.7	96.9±1.3
Volumetric shrinkage (%)	61.2±1.6	5.2±3.7	57.2±1.4
Densification ratio (%)	83.9±2.3	7.1±1.0	94.5±1.9

Figure 7. The green bulk density and sinterability metrics of the three powders

4. CONCLUSIONS

Three different feedstock powders for the binder jetting additive manufacturing process, i.e., fine raw powder, coarse raw powder, and granulated powder, were compared in terms of flowability and sinterability. The granulated powder was prepared by spray freeze granulation, which provided spherical shape and porous structure. Various flowability metrics were measured, including volumetric flow rate, mass flow rate, Hausner ratio, Carr index, and repose angle. Then disk samples were pressed and sintered for each powder. Different sinterability metrics were measured and calculated, including sintered bulk density, volumetric shrinkage, and densification ratio. The granulated powder achieved comparable flowability metrics to the coarse raw powder due to their similar size (i.e., ~70 μm) and shape (spherical). The granulated powder showed similar sinterability to the fine raw powder due to the same original particle size (i.e., 300 nm). Fine raw powder has very low flowability as a result of its large inter-agglomerate/particle forces. The coarse raw powder has very low sinterability as a result of its large particle size and thus low sintering driving force. Moreover, the volumetric and mass flow rates are not suitable flowability metrics for the comparison of these three powders. Reasons include the incapacity to measure corresponding values for the fine raw powder and the underestimation of the flowability for the granulated powder. Volumetric shrinkage and densification ratio are better sinterability metrics than sintered bulk density as they are not significantly dependent on the green density. This study provides guidance for assessing and selecting the feedstock powder for ceramic binder jetting additive manufacturing.

REFERENCES

[1]   Du, W., Ren, X., Ma, C., and Pei, Z., 2017, "Binder Jetting Additive Manufacturing of Ceramics: A Literature Review," *Proceedings of the ASME 2017*

International Mechanical Engineering Congress and Exposition, Tampa, FL, pp. 1–12.

[2] Klocke, F., 1997, "Modern Approaches for the Production of Ceramic Components," Journal of the European Ceramic Society, 17(2–3), pp. 457–465.

[3] Deckers, J., Vleugels, J., and Kruth, J. P., 2014, "Additive Manufacturing of Ceramics: A Review," Journal of Ceramic Science and Technology, 5(4), pp. 245–260.

[4] Du, W., Ren, X., Ma, C., and Pei, Z., 2019, "Ceramic Binder Jetting Additive Manufacturing: Particle Coating for Increasing Powder Sinterability and Part Strength," Materials Letters, 234, pp. 327–330.

[5] Du, W., Ren, X., Chen, Y., Ma, C., Radovic, M., and Pei, Z., 2018, "Model Guided Mixing of Ceramic Powders with Graded Particle Sizes in Binder Jetting Additive Manufacturing," *Proceedings of the ASME 2018 13th International Manufacturing Science and Engineering Conference*, College Station, TX, pp. 1–9.

[6] Zocca, A., Gomes, C. M., Staude, A., Bernardo, E., Günster, J., and Colombo, P., 2013, "SiOC Ceramics with Ordered Porosity by 3D-Printing of a Preceramic Polymer," Journal of Materials Research, 28(17), pp. 2243–2252.

[7] Zocca, A., Elsayed, H., Bernardo, E., Gomes, C. M., Lopez-Heredia, M. A., Knabe, C., Colombo, P., and Günster, J., 2015, "3D-Printed Silicate Porous Bioceramics Using a Non-Sacrificial Preceramic Polymer Binder," Biofabrication, 7(2), p. 25008.

[8] Zocca, A., Gomes, C. M., Bernardo, E., Muller, R., Gunster, J., and Colombo, P., 2013, "LAS Glass-ceramic Scaffolds by Three-Dimensional Printing," Journal of the European Ceramic Society, 33(9), pp. 1525–1533.

[9] Miyanaji, H., Zhang, S., Lassell, A., Zandinejad, A. A., and Yang, L., 2016, "Optimal Process Parameters for 3D Printing of Porcelain Structures," Procedia Manufacturing, 5, pp. 870–887.

[10] Nan, B., Yin, X., Zhang, L., and Cheng, L., 2011, "Three-Dimensional Printing of Ti3SiC2-based Ceramics," Journal of the American Ceramic Society, 94(4), pp. 969–972.

[11] Yin, X., Travitzky, N., Melcher, R., and Greil, P., 2006, "Three-Dimensional Printing of TiAl3/Al2O3 Composites," Zeitschrift für Metallkunde, 97(5), pp. 492–498.

[12] Travitzky, N. ., and Shlayen, A., 1998, "Microstructure and Mechanical Properties of Al2O3/Cu–O Composites Fabricated by Pressureless Infiltration Technique," Material Science and Engineering A, 244(2), pp. 154–160.

[13] Fu, Z., Schlier, L., Travitzky, N., and Greil, P., 2013, "Three-dimensional Printing of SiSiC Lattice Truss Structures," Materials Science and Engineering A, 560, pp. 851–856.

[14] ISO, 2013, "ISO 18754:2013 Fine Ceramics (Advanced Ceramics, Advanced Technical Ceramics) – Determination of Density and Apparent Porosity."

[15] Mehrban, N., Bowen, J., Vorndran, E., Gbureck, U., and Grover, L. M., 2013, "Structural Changes to Resorbable Calcium Phosphate Bioceramic Aged in Vitro," Colloids and Surfaces B: Biointerfaces, 111, pp. 469–478.

[16] Sheydaeian, E., Vlasea, M., Woo, A., Pilliar, R., Hu, E., and Toyserkani, E., 2016, "Effect of Glycerol Concentrations on the Mechanical Properties of Additive Manufactured Porous Calcium Polyphosphate Structures for Bone Substitute Applications," Journal of Biomedical Materials Research Part B: Applied Biomaterials, pp. 828–835.

[17] Dcosta, D. J., Sun, W., Lin, F., and Ei-Raghy, T., 2002, "Freeform Fabrication of Ti3SiC2 Powder-based Structures: Part II - Characterization and Microstructure Evaluation," Journal of Materials Processing Technology, 127(3), pp. 352–360.

[18] Shanjani, Y., Amritha De Croos, J. N., Pilliar, R. M., Kandel, R. A., and Toyserkani, E., 2010, "Solid Freeform Fabrication and Characterization of Porous Calcium Polyphosphate Structures for Tissue Engineering Purposes," Journal of Biomedical Materials Research Part B: Applied Biomaterials, 93(2), pp. 510–519.

[19] Tarafder, S., Balla, V. K., Davies, N. M., Bandyopadhyay, A., and Bose, S., 2013, "Microwave-sintered 3D Printed Tricalcium Phosphate Scaffolds for Bone Tissue Engineering," Journal of Tissue Engineering and Regenerative Medicine, 7(8), pp. 631–641.

[20] Suwanprateeb, J., Sanngam, R., and Suwanpreuk, W., 2008, "Fabrication of Bioactive Hydroxyapatite/Bis-GMA Based Composite via Three Dimensional Printing," Journal of Materials Science: Materials in Medicine, 19(7), pp. 2637–2645.

[21] Suwanprateeb, J., Sanngam, R., and Panyathanmaporn, T., 2010, "Influence of Raw Powder Preparation Routes on Properties of Hydroxyapatite Fabricated by 3D Printing Technique," Materials Science and Engineering C, 30(4), pp. 610–617.

[22] Warnke, P. H., Seitz, H., Warnke, F., Becker, S. T., Sivananthan, S., Sherry, E., Liu, Q., Wiltfang, J., and Douglas, T., 2010, "Ceramic Scaffolds Produced by Computer-assisted 3D Printing and Sintering: Characterization and Biocompatibility Investigations," Journal of Biomedical Materials Research Part B: Applied Biomaterials, 93(1), pp. 212–217.

[23] Birkholz, M. N., Agrawal, G., Bergmann, C., Schröder, R., Lechner, S. J., Pich, A., and Fischer, H., 2015, "Calcium Phosphate/Microgel Composites for 3D Powderbed Printing of Ceramic Materials," Biomedizinische Technik, 61(3), pp. 267–279.

[24] Seidenstuecker, M., Kerr, L., Bernstein, A., Mayr, H., Suedkamp, N., Gadow, R., Krieg, P., Hernandez Latorre, S., Thomann, R., Syrowatka, F., and Esslinger, S., 2017, "3D Powder Printed Bioglass and β-tricalcium

Phosphate Bone Scaffolds," Materials, 11(1), p. 13.

[25] Raghupathy, B. P. C., and Binner, J. G. P., 2011, "Spray Granulation of Nanometric Zirconia Particles," Journal of the American Ceramic Society, 94(1), pp. 42–48.

[26] Zhang, Y., Binner, J., Rielly, C., and Vaidhyanathan, B., 2014, "Comparison of Spray Freeze Dried Nanozirconia Granules Using Ultrasonication and Twin-fluid Atomisation," Journal of the European Ceramic Society, 34(4), pp. 1001–1008.

[27] Binner, J., and Vaidhyanathan, B., 2008, "Processing of Bulk Nanostructured Ceramics," Journal of the European Ceramic Society, 28(7), pp. 1329–1339.

[28] Ho, T. M., and Truong, T., 2017, "Spray-drying and Non-equilibrium States/Glass Transition," *Non-Equilibrium States and Glass Transitions in Foods*, Woodhead Publishing, Duxford, pp. 111–136.

[29] Irsen, S. H., Leukers, B., Höckling, C., Tille, C., and Seitz, H., 2006, "Bioceramic Granulates for Use in 3D Printing: Process Engineering Aspects," Materialwissenschaft und Werkstofftechnik, 37(6), pp. 533–537.

[30] ISO, 2014, "ISO 9276-2:2014 - Representation of Results of Particle Size Analysis -- Part 2: Calculation of Average Particle Sizes/Diameters and Moments from Particle Size Distributions."

[31] Spath, S., and Seitz, H., 2014, "Influence of Grain Size and Grain-Size Distribution on Workability of Granules with 3D Printing," The International Journal of Advanced Manufacturing Technology, 70(1–4), pp. 135–144.

[32] ASTM International, 2013, "B212-13: Standard Test Method for Apparent Density of Free-flowing Metal Powders Using the Hall Flowmeter Funnel."

[33] ASTM International, 2013, "B417 2013: Standard Test Method for Apparent Density of Non-free-flowing Metal Powders Using the Carney Funnel."

[34] Yang, R. Y., Zou, R. P., and Yu, A. B., 2000, "Computer Simulation of the Packing of Fine Particles," Physical Review E, 62(3), pp. 3900–3908.

[35] Kang, S.-J. L., 2005, *Sintering : Densification, Grain Growth, and Microstructure*, Elsevier Butterworth-Heinemann, Burlington.

[36] Zhu, S., Fahrenholtz, W. G., and Hilmas, G. E., 2007, "Influence of Silicon Carbide Particle Size on the Microstructure and Mechanical Properties of Zirconium Diboride-silicon Carbide Ceramics," Journal of the European Ceramic Society, 27(4), pp. 2077–2083.